OPTICS

Broadband and efficient third-harmonic generation from black phosphorus–hybrid plasmonic metasurfaces in the mid-infrared

Song Zhu[1,2]†, Wenduo Chen[1]†, Tugba Temel[1,3]†, Fakun Wang[1], Xiaodong Xu[4], Ruihuan Duan[5], Tingting Wu[1], Xuan Mao[1], Congliao Yan[1], Jianbo Yu[1], Chongwu Wang[1], Yuhao Jin[1], Jieyuan Cui[1], Jinghao Li[1], Dora Juan Juan Hu[6], Zheng Liu[5], Robert T. Murray[3]*, Yu Luo[2]*, Qi Jie Wang[1,7]*

Black phosphorus (BP), with a mid-infrared (MIR) bandgap of 0.34 eV, presents itself as a promising material for MIR nonlinear optical applications. We report the realization of MIR third-harmonic generation (THG) in both BP and BP-hybrid plasmonic metasurfaces (BPM). BP exhibits a high third-order nonlinear susceptibility ($\chi^{(3)}$) exceeding 10^{-18} m^2/V^2 in the MIR region with a maximum value of 1.55×10^{-17} m^2/V^2 at 5000 nm. The BP flake achieves a THG conversion efficiency of 1.4×10^{-5}, surpassing that of other 2D materials by over one order of magnitude. To further enhance this nonlinear performance, a BPM is designed and fabricated to achieve a two-order-of-magnitude enhancement in THG, leading to a record conversion efficiency of 6.5×10^{-4}, exceeding the performance of previously reported metasurfaces by more than one order of magnitude. These findings establish BP as a promising platform for next-generation MIR nonlinear optical devices.

INTRODUCTION

High-performance mid-infrared (MIR) nonlinear optical materials are of great importance for emerging nonlinear optical applications, including tunable MIR coherent sources (*1*), frequency up-conversion photodetection and imaging (*2*), and MIR frequency comb–based spectroscopy (*3*). Among these nonlinear optical processes, third-harmonic generation (THG) in the MIR region plays a critical role in detecting molecules resonance (*4*), probing intraband transitions in the quantum structures (*5*), and enabling MIR up-conversion imaging (*6*). While THG in the MIR has been explored in various materials systems such as germanium (*7*) and phase-change material (*8*), achieving broadband and highly efficient nonlinear frequency conversion remains a challenge for ultrafast photonics, frequency conversion, and on-chip nonlinear optics in the MIR regime, necessitating the research into novel material platforms.

Two-dimensional (2D) van der Waals materials have recently emerged as promising candidates for nanoscale nonlinear optics due to their exceptionally high nonlinear coefficients (*9*–*11*), outperforming traditional bulk materials. Investing MIR THG in these materials not only enables the detection of fundamental band transitions, as demonstrated in graphene (*12*) and PtS_2 (*13*) but also provides insight into their third-order susceptibilities ($\chi^{(3)}$), enabling advanced nonlinear applications such as four-wave mixing and the Kerr-based integrated photonics (*14*, *15*). However, most studies on the nonlinear optics of 2D materials have primarily focused on the visible to near-infrared (NIR) spectral range (*9*, *14*, *16*), with few 2D materials exhibiting strong nonlinear responses in the MIR region. Graphene, for instance, has $\chi^{(3)}$ values on the order of 10^{-17} m^2/V^2 at 3100 nm but suffers from limited THG conversion efficiency due to its atomic-scale thickness (*12*). Black phosphorus (BP), a layered van der Waals material with a widely tunable bandgap from the visible (1.8 eV in monolayer) to MIR (0.34 eV in bulk), has been extensively explored for applications in MIR photodetection (*17*), modulators (*18*), light sources (*19*, *20*), and nonlinear optics (*21*–*23*). Its MIR bandgap offers unique opportunities for enhancing third-order nonlinear processes, yet this potential remains largely unexplored, with prior nonlinear optical studies of BP flakes restricted to wavelengths below 1550 nm.

A major challenge in applying van der Waals layered materials for nonlinear frequency conversion is their intrinsically low conversion efficiency due to limited interaction volumes. Micro- and nanophotonic structures, including metamaterials (*24*, *25*), waveguides (*26*–*28*), and optical cavities (*29*, *30*), have been used to overcome this limitation by enhancing local field intensities. In particular, plasmonic metasurfaces are highly effective in amplifying nonlinear optical responses by confining light into subwavelength volumes with highly enhanced local electric fields (*24*, *25*, *31*). Compared to conventional metasurfaces, metal-insulator-metal (MIM) plasmonic architectures offer superior field enhancement and larger interaction volumes within the dielectric layer, making them particularly advantageous for boosting nonlinear processes in thick van der Waals flakes such as BP (*31*, *32*).

In this work, we present the experimental demonstration of broadband and highly efficient MIR nonlinear processes in BP and the BP-hybrid plasmonic metasurface (BPM) via THG. We reveal that BP exhibits remarkable large $\chi^{(3)}$ values exceeding 10^{-18} m^2/V^2 in the MIR region from 3000 to 5000 nm, attributed to multiphoton transition resonances (*12*). $\chi^{(3)}$ increases monotonically with wavelength, reaching a peak value of 1.55×10^{-17} m^2/V^2 at 5000 nm, enabling a record THG conversion efficiency of 1.4×10^{-5}, which is

[1]School of Electrical and Electronic Engineering, Nanyang Technological University, 639798 Singapore, Singapore. [2]National Key Laboratory of Microwave Photonics, Nanjing University of Aeronautics and Astronautics, Nanjing, China. [3]Blackett Laboratory, Department of Physics, Imperial College London, London SW7 2BW, United Kingdom. [4]School of Materials Science and Engineering, Harbin Institute of Technology, Harbin 150001, China. [5]School of Materials Science and Engineering, Nanyang Technological University, 639798 Singapore, Singapore. [6]Agency for Science, Technology and Research (A*STAR), Institute for Infocomm Research (I2R), 138632 Singapore, Singapore. [7]School of Physical and Mathematical Sciences, Nanyang Technological University, 637371 Singapore, Singapore.
*Corresponding author. Email: qjwang@ntu.edu.sg (Q.J.W.); yu.luo@nuaa.edu.cn (Y.L.); robert.murray10@imperial.ac.uk (R.T.M.)
†These authors contributed equally to this work.

over one order of magnitude higher than that of other 2D materials. To further enhance THG performance, we design and fabricate a MIR BPM that achieves a two-order-of-magnitude enhancement in THG intensity over a broad spectral range from 3000 to 4000 nm. The BPM yields a maximum enhancement factor of ~170 at 3500 nm, resulting in an effective nonlinear susceptibility ($\chi^{(3)}_{eff}$) exceeding 10^{-17} m^2/V^2 across the entire 3000 to 5000 nm range. This unprecedented enhancement leads to a record-high THG conversion efficiency of 6.5×10^{-4} in a 50-nm BP flake at 3500 nm, surpassing the best-performing metasurfaces reported to date by over one order of magnitude (*33*). Our findings establish BP as a promising platform for MIR nonlinear nanophotonics, providing a compelling route toward high-efficiency ultrafast photonic devices, frequency conversion technologies, and integrated nonlinear optics. This work not only expands the fundamental understanding of MIR nonlinearities in BP but also paves the way for next-generation nonlinear optical components with record-breaking performance.

RESULTS

THG processes from BP in the MIR region

Figure 1A presents the schematic structure of a single unit cell of the BPM, which consists of three key components: a bottom gold (Au) layer, a dielectric spacer, and an Au dimer antenna with a nanoscale gap. As shown in Fig. 1B, the dielectric layer consists of a ~7-nm layer of aluminum oxide (Al_2O_3) along with a BP flake. The structural anisotropy of the BP crystal, indicated by the distinction between the armchair (AC) and zigzag (ZZ) crystallographic directions, gives rise to anisotropic band transitions (*20*), as depicted in Fig. 1C. Atomic force microscopy (AFM) analysis confirms a BP flake thickness of 38 nm (Fig. 1D). Furthermore, the absorption band-edge and anisotropic absorbance of the BP flake are experimentally validated across multiple wavelengths (1500, 2500, 3000, and 4200 nm) (note S1 and fig. S2). The absorption spectrum reveals a band-edge absorption at ~3600 nm, corresponding to a photon energy of ~0.34 eV (Fig. 1E). Anisotropic absorbance measurements show maximum absorption along the AC direction, with negligible absorption along the ZZ direction (Fig. 1F).

The THG processes are characterized using an optical setup incorporating both reflection and transmission configurations (Fig. 2A and Materials and Methods). The emission spectrum of the third-harmonic light at 1220 nm from fundamental excitation at 3660 nm is shown in Fig. 2C. Power-dependent measurements show a characteristic cubic dependence (slope = 2.9) on the excitation power, consistent with perturbative nonlinear optical behavior (inset in Fig. 2C) (*22*). Given that the BP bandgap (~0.34 eV) aligns with a fundamental wavelength of ~3647 nm, wavelength-dependent THG experiments are performed within the 3600 to 3900 nm range (Fig. 2D). The THG intensity exhibits a monotonic increase as the fundamental wavelength increases. For a deeper insight into the wavelength-dependent THG in the MIR region, the nonlinear susceptibility ($\chi^{(3)}$) is evaluated over a broadband spectral range (1500 to 5000 nm) (Fig. 2E and Materials and Methods). We find that the $\chi^{(3)}$ value of BP at 1550 nm is ~2×10^{-19} m^2/V^2, consistent with prior reports on bulk BP (*21*, *22*). In the MIR region, $\chi^{(3)}$ values reach 5.88×10^{-18} m^2/V^2 at 3250 nm, 10.4×10^{-18} m^2/V^2 at 4000 nm, and 15.5×10^{-18} m^2/V^2 at 5000 nm, exceeding the values at 1550 nm by one to two orders of magnitude. These values surpass those in conventional nonlinear optical materials, including various 2D and bulk materials, and are comparable to those observed in monolayer graphene (table S1). This enhancement can be attributed to mixed contributions by the interband and intraband transitions within the two-band system of BP, which facilitates multiphoton transition resonance (Fig. 2B, notes S4 and S5, and fig. S9). These multiphoton transitions correspond to incident photon energies of $\hbar\omega = E_g$, $\hbar\omega = E_g/2$, and $\hbar\omega = E_g/3$, same as the transition processes in monolayer graphene (*12*).

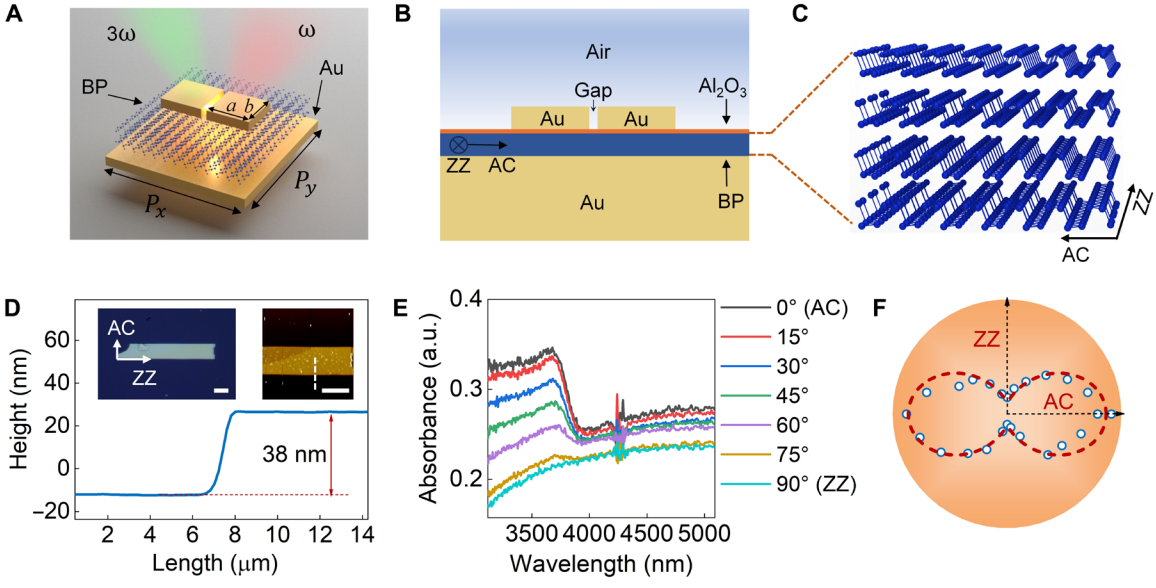

Fig. 1. BPM and optical characterization. (**A**) Schematic diagram of the BPM. *a* and *b* are the length and width of a single antenna in the dimer structure, respectively. P_x and P_y represent the periods in the AC and ZZ directions of BP, respectively. (**B**) Cross-sectional geometry of the BPM. (**C**) 3D crystal structure of BP. (**D**) AFM profile of the BP flake. The left inset: optical image of the BP flake. Scale bar, 15 μm; the right inset: AFM image of the BP flake. Scale bar, 15 μm. (**E**) Polarized absorption of the BP flake in the MIR region. (**F**) Angle-resolved absorption around the band-edge from the BP flake. The dashed line represents the fitted curve derived from the experimental data.

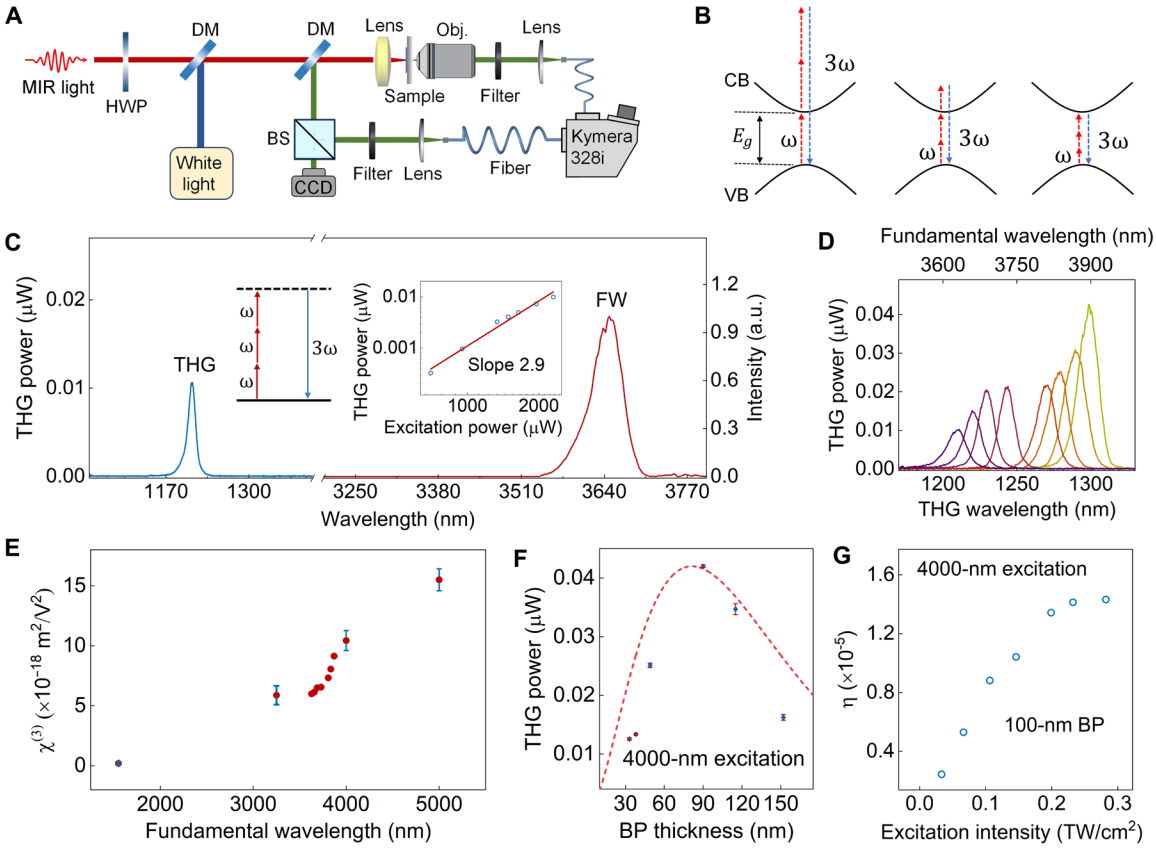

Fig. 2. THG measurements of BP flakes under MIR excitation. (**A**) Experimental setup for THG measurements through reflection and transmission configurations. HWP, half-wave plate; DM, dichroic mirror; BS, beam splitter; Obj., objective; CCD, charge-coupled device. (**B**) Multiphoton resonances for THG processes in BP with the two-band system. The red arrows represent the fundamental photon at ω and the blue arrow represents the THG photons at 3ω. CB, conduction band; VB, valence band; E_g, bandgap. (**C**) Spectra of the fundamental wave (FW) at ~3660 nm (right axis) and the THG signal at ~1220 nm (left axis) under 2.3-mW excitation. Left inset, schematic diagram of the THG process; right inset, log-log plot between the THG intensity and the excitation power. (**D**) THG spectra at different fundamental wavelengths across the MIR region from 3600 to 3900 nm under 3-mW excitation. (**E**) Experimentally extracted $\chi^{(3)}$ values of the BP from the NIR to MIR (1550 to 5000 nm) regions. The$\chi^{(3)}$ values (red dots) between 3600 to 4000 nm are extracted from (D). (**F**) Thickness-dependent THG intensity in the transmission configuration under 3-mW excitation. The error bars and dashed line represent experimental and calculated results from Eq. 1. (**G**) THG conversion efficiency (η) versus the excitation intensity under 4000-nm excitation.

The observed $\chi^{(3)}$ dispersion closely aligns with the theoretical predications based on the density functional theory in combination with the Wannier interpolation method (note S4 and fig. S9). Minor discrepancies may stem from the crystalline quality of the BP flakes used in the experiments.

To further investigate THG behavior, thickness-dependent THG measurements are performed using the transmission configuration (Fig. 2A). Since BP exhibits negligible absorption at ~4000 nm due to its lower photon energy relative to its bandgap, thickness-dependent THG is conducted at this wavelength. The coherence length (L_{coh}) between the fundamental and forward propagating third-harmonic waves is calculated to be ~950 nm using the equation (*21*): $L_{coh} = \lambda / 6\left(n_\omega - n_{3\omega}\right)$, where $\lambda = 4000$ nm represents the fundamental wavelength, $n_\omega = 4.2$ and $n_{3\omega} = 3.5$ are refractive indices (RIs) at the fundamental and THG wavelengths, respectively (*34*). Given that the coherence length substantially exceeds the used BP thickness (typically at 100 nm or thinner), the THG intensity initially increases with the BP thickness, reaching a maximum at ~90 nm, before experiencing attenuation due to strong optical absorption at the THG wavelength (Fig. 2F). The experimental results can be well fitted using the following equation (*21*)

$$I_{3\omega}(l) \propto |\chi^{(3)}|^2 I_\omega^3 \left[\frac{e^{-2\alpha l} - 2\cos(\Delta k l)e^{-\alpha l} + 1}{\alpha^2 + \Delta k^2}\right] e^{-2\alpha l} \quad (1)$$

where I_ω and $I_{3\omega}$ represent the excitation and THG intensities, respectively, l is the thickness of the BP flake, αdenotes the absorption coefficient of the THG signal, and Δk is the phase-mismatch parameter between the fundamental wavelength and the THG wavelength (Materials and Methods).

Here, we investigate THG conversion efficiency for a ~100-nm BP flake under 4000-nm excitation, corresponding to the peak THG intensity (Fig. 2, F and G). The efficiency exhibits a gradual increase with increasing excitation intensity before saturating at ~0.2 TW/cm^2, primarily due to two-photon absorption leading to fundamental light depletion (*35*, *36*). A maximum THG conversion efficiency ($\eta = P^{3\omega} / P^{\omega}$, where P^{ω} is the incident power of the fundamental light, while $P^{3\omega}$ represents the THG power output from BP accounting

for absorption and reflection effects of the BP flake) of 1.4×10^{-5} is achieved at an excitation intensity of 0.3 TW/cm^2, surpassing values observed in commonly used 2D van der Waals materials by over an order of magnitude (table S1). THG conversion efficiency at 4000 nm is six orders of magnitude larger than that of monolayer graphene (at 3100 nm), despite comparable $\chi^{(3)}$ values in both materials (*12*). The high enhancement is primarily attributed to BP's intrinsically high $\chi^{(3)}$ in the MIR region, which remains independent of flake thickness (Fig. 2E).

Extreme polarization anisotropy for THG in the MIR region

BP displays pronounced optical anisotropy due to its intrinsic in-plane asymmetry between the AC and ZZ directions (Fig. 1, E and F) (*37*). To investigate this anisotropy, we study in-plane polarized THG across the MIR region (Fig. 3). The in-plane THG anisotropy is quantified by the ratio I_{AC}/I_{ZZ}, where I_{AC} and I_{ZZ} represent the THG intensities generated when the excitation light is polarized along the AC and ZZ directions, respectively. The THG spectra are measured for fundamental excitations ranging from 1400 nm to 5000 nm (Fig. 3, A to C, and fig. S6). The THG anisotropy in the BP flake has values of ~2.5 under 1400-nm excitation and increases to ~50 at 3500 nm. It is worth noting that for excitation wavelengths exceeding 3500 nm, the THG signal along the ZZ direction becomes negligible compared to that along the AC direction, demonstrating an extreme polarization anisotropy comparable to that observed in 1D carbon nanotubes (*38*). Since the excitation light is normally incident on the BP flake, the THG process is primarily governed by four independent third-order susceptibility tensor elements (χ_{11}, χ_{22}, χ_{18}, and χ_{29}) (note S3). Angle-resolved THG measurements at different excitation wavelengths (Fig. 3, D to G) reveal a pronounced evolution in the polarization-dependent intensity profiles, which are well fitted by eq. S3. This evolution is attributed to wavelength-dependent variations in the relative magnitudes of χ_{11}, χ_{22}, χ_{18}, and χ_{29}. Specifically, the dispersion behaviors of χ_{11} (χ_{xxxx}), χ_{22} (χ_{yyyy}), χ_{18} (χ_{xxyy}), and χ_{29} (χ_{yxxy}) varies across the MIR region, influencing the observed THG anisotropy. The dominant contribution to THG arises from the χ_{11}, χ_{18}, and χ_{29} elements, which are associated with the E_x component along the AC direction. In contrast, χ_{22} (χ_{yyyy}), which corresponds to the ZZ direction, shows negligible dispersion due to the absence of transition resonance along this axis. Figure 3H shows the retrieved relative magnitudes of χ_{11}, χ_{22}, χ_{18}, and χ_{29} as a function of the excitation wavelength. While χ_{18} and χ_{29} remain within a range of 0.3 to 0.53 across 1400 to 5000 nm, χ_{22} becomes negligible relative to χ_{11} beyond 3500 nm. This behavior arises from the enhanced multiphoton resonance along the AC direction in the MIR region. Furthermore, thickness-dependent analyses indicate that χ_{11} remains largely invariant for BP flakes exceeding 10 nm in thickness, as the band structure undergoes minimal modifications beyond this threshold (Fig. 3I) (*39*). The extreme polarization anisotropy observed in BP confirms that χ_{11} is the dominant component of the third-order nonlinear susceptibility ($\chi^{(3)}$) in the MIR region, resulting in a highly directional THG signal for excitation polarized along the AC axis. This behavior is in stark contrast to the nearly isotropic THG observed in group VI transition metal dichalcogenides (e.g., MoS_2) (*40*). Furthermore, BP's THG anisotropy surpasses that of other asymmetric 2D materials (*41*),

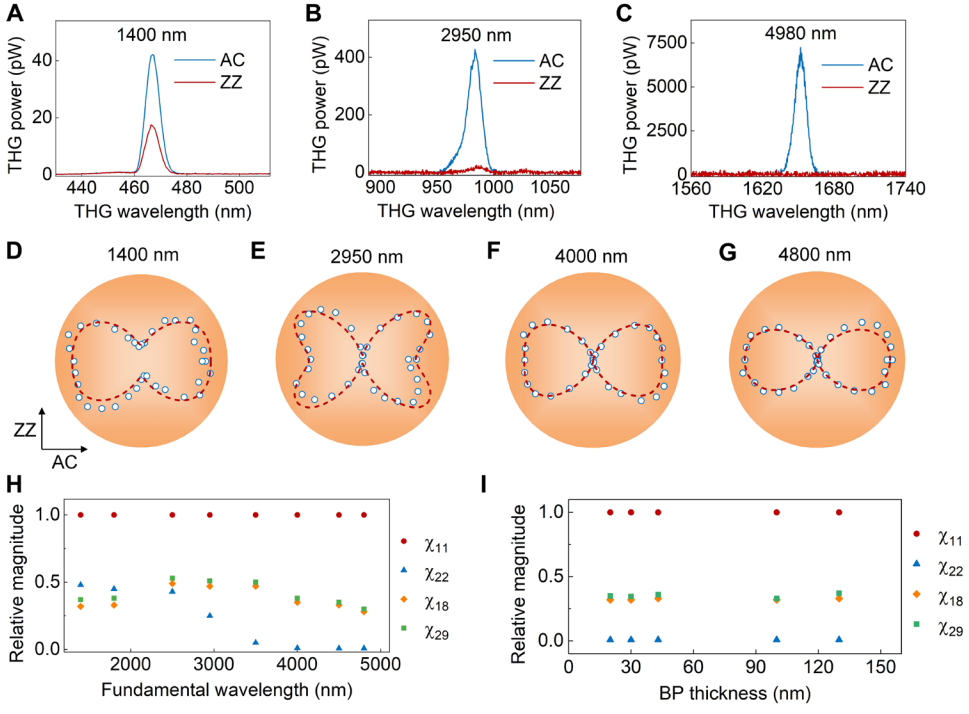

Fig. 3. Polarization-dependent THG progresses in the BP flake. (**A** to **C**) THG spectra for the light polarization along AC (blue) and ZZ (red) directions under 1400-nm (power, 0.58 mW), 2950-nm (power, 7 mW), and 4980-nm (power, 5.6 mW) excitations, respectively. (**D** to **G**) Polar plots of the THG intensity versus the polarization angle under 1400-, 2950-, 4000-, and 4800-nm excitations, respectively. (**H**) Retrieved relative magnitudes of χ_{11}, χ_{22}, χ_{18}, and χ_{29} as a function of the fundamental wavelength. The red lines are calculated by eq. S3. (**I**) Retrieved relative magnitudes of χ_{11}, χ_{22}, χ_{18}, and χ_{29} as a function of the BP thickness.

highlighting its potential for polarization-sensitive nonlinear photonic applications.

Enhanced THG processes by the BPM

To further enhance THG performance of BP in the MIR region, we design and fabricate a BPM. The local electric field enhancement in the BPM at 3500 nm is first analyzed through the finite-difference time-domain (FDTD) simulations (Fig. 4, A to C, and Materials and Methods). Figure 4A shows the x component (E_x) of the local electric field in the x-z cross section of the dimer and dielectric layer, revealing a 67-fold enhancement in the dimer gap region. Since BP serves as the primary material in the dielectric layer of the MIM plasmonic structure, it is necessary to analyze the electric field distribution in the BP flake. Figure 4 (B and C) shows the electric field distributions of the x and z components in the x-z cross section of the BP layer, demonstrating a 14-fold enhancement in the E_x component on the BP surface due to the combined effects of the dimer gap and the reflective bottom Au layer. An exceptional decay of the electric field from the top surface of the BP layer is observed when the dimer gap is 30 nm, as depicted by the orange dashed line in Fig. 4D. The electric field permeates over 20 nm into the BP flake before decaying to $1/e$ of its maximum value. Given the challenge of obtaining large, high-quality BP flakes thinner than 50 nm, a 50-nm BP flake is used for metasurface fabrication. Comparations with a metal-insulator (MI) plasmonic metasurface (fig. S14) indicate that the maximum E_x enhancement in the MI structure is only 3.2-fold, over four times lower than that in the MIM-based BPM (Fig. 4D). Besides, the E_z component is enhanced by 27-fold at the BP surface (Fig. 4C). However, χ_{16} and χ_{24} are much smaller than χ_{11} due to the absence of resonance absorption in the out-of-plane direction of BP, the enhancement of E_x is the primary factor driving THG enhancement. The dimer gap affects the electric field distribution in the dielectric layer. Simulations of BPMs with varying dimer gaps (20, 30, 60, 100, and 150 nm) (Fig. 4D and fig. S13) confirm that a smaller gap results in higher electric field enhancement in BP and consequently greater THG enhancement (*42*). Because of limitations in the minimum gap possible with our fabrication process, a dimer gap of ~30 nm is designed and fabricated in this work. However, it is important to note that excessively confining the electric field within the dimer gap by continuously reducing the gap size is not advisable, as excessive field confinement leads to a decrease in the THG intensity and the conversion efficiency (note S6 and fig. S12).

The BPM is fabricated using a standard lift-off process (Materials and Methods). The fabricated metasurface has an effective size of ~33 μm × 40 μm, exceeding the focused beam diameter (~30 μm) of the incident light (Fig. 4E). A scanning electron microscopy (SEM) image of a unit cell (Fig. 4F) shows a dimer structure with a gap of ~34 nm, with individual antennas measuring 480 nm in length and 198 nm in width. To maximize THG along the AC direction, where χ_{11} is the highest, the dimer orientation is aligned parallel to the AC direction of the BP flake (Fig. 1B). Since BP is sensitive to water and oxygen, an Al_2O_3 protective layer is deposited before metasurface fabrication (Materials and Methods and fig. S8). AFM analysis confirms the BP flake thickness (~50 nm) and dielectric layer thickness (~57 nm) (Fig. 4G). Raman spectroscopy verifies that BP remains undamaged throughout fabrication, as no shift in Raman peak positions is observed (Fig. 4H).

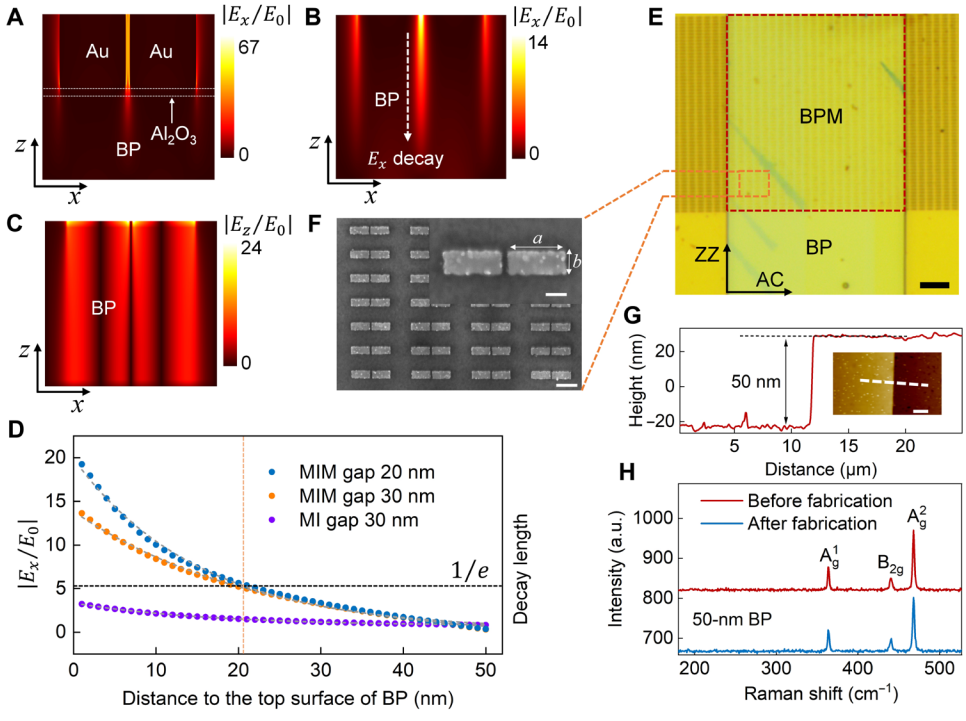

Fig. 4. Design and fabrication of the BPM. (**A**) Simulated E_x component of the BPM in the x-z cross section of the domain from BP to the dimer in one unit cell. (**B**) E_x component in the x-z cross section of 50-nm BP. (**C**) E_z component in the x-z cross section of 50-nm BP. (**D**) Decay of the enhanced electric fields (E_x / E_0) versus the distance to the top surface of BP in the MIM and MI metasurfaces with different dimer gaps. (**E**) Optical image of the BPM acquired by the optical microscope. Scale bar, 5 μm. (**F**) Top view of the SEM image of the fabricated BPM (scale bar, 500 nm). Inset: SEM image of a unit cell (scale bar, 200 nm). (**G**) AFM profile of the BP flake used for metasurface fabrication. Inset: AFM image of the BP flake. Scale bar, 2 μm. (**H**) Raman characterization of the BP flake before and after fabrication.

Figure 5A shows the reflection spectra of the BPM and a bare BP flake (~50 nm thick). A pronounced resonance dip appears at 3500 nm in the BPM under AC-polarized light, while the bare BP flake exhibits negligible absorption. The negligible absorption from the bare BP arises from the measurement in a small area (<30 μm × 30 μm), which is comparable to the metasurface size, limiting its absorption (note S7 and fig. S16). There is negligible resonance dip when the linear polarized light is along the ZZ direction, confirming the anisotropic nature of the BPM. To verify THG enhancement, power-dependent THG measurements of the BPM at varying polarization angles confirm the expected cubic dependence on the excitation power (Fig. 5B). The polarization-dependent THG intensities are also analyzed (note S8 and fig. S17). The results demonstrate that the line shape is strongly dependent on the rotation angle and show strong anisotropy due to the directional electric field enhancement of the BPM. THG spectra under different excitation polarizations at a fixed excitation power of (~6 mW) are shown in Fig. 5C. THG signal is negligible when the excitation polarization is along the ZZ direction by comparing to that from the bare BP flake (fig. S6D). Figure 5D shows the corresponding THG signals as the bare BP flake and BPM are excited by the fundamental light with a central wavelength of ~3500 nm. A 170-fold enhancement is observed since the incident light is highly enhanced at 3500 nm, which fully demonstrates the strong plasmonic enhancement of third-order optical nonlinearity of BP.

Wavelength-dependent THG enhancement is further investigated by tuning the fundamental wavelength from 2500 to 4650 nm (Fig. 5E). The THG enhancement increases from 3000 nm (~46-fold), reaching its maximum (~170-fold) around 3500 nm, before gradually decreasing to ~17-fold at approximately 4000 nm. However, the THG enhancements are only ~6 at 2500 nm and ~3 at 4650 nm, as the electric field enhancement is much weaker than that at 3500 nm due to the large wavelength detuning from the resonance (Fig. 5A). Simulations confirm that the BPM exhibits maximum electric field enhancement at ~3500 nm, while showing lower enhancement at ~3000 nm (fig. S15). The effective nonlinear susceptibility $\left(\chi_{\mathrm{eff}}^{(3)}\right)$ of BP in the BPM is calculated over the wavelength range of 3000 to 4000 nm based on the equation (*43*): $|\chi_{\mathrm{eff}}^{(3)}| = \sqrt{\frac{I_{\mathrm{BPM}}}{I_{\mathrm{BP}}}}\,|\chi^{(3)}|$, where I_{BPM} and I_{BP} are the THG intensities from the BPM and bare BP flake at the same excitation power. Because of the strong plasmonic enhancement and intrinsic nonlinearity of BP, $\chi_{\mathrm{eff}}^{(3)}$ exceeds 10^{-17} m^2/V^2 over a broadband spectral range from 3000 to 5000 nm (Fig. 5F). The performance in the MIR region surpasses that of other 2D materials by one to two orders of magnitude (10 to 100 times), as detailed in table S1. The THG conversion efficiency is also enhanced by ~170-fold at 3500 nm. The THG conversion efficiency at 3500 nm is also investigated in the 50-nm BP flake (note S9 and figs. S21 and S22). The results indicate that the THG conversion efficiency of BP in the reflection configuration is 1.84×10^{-6} at a maximum excitation intensity of 0.044 TW/cm^2, corresponding to a peak efficiency of 3.16×10^{-4} from the BPM. This value corresponds to 86% of that in the transmission configuration. The maximum THG conversion efficiency of 4.4×10^{-6} in the transmission configuration is achieved at an excitation intensity of 0.17 TW/cm^2 using a reflective objective (LMM40X-P01). Considering the efficiency ratio (with 86% efficiency ratio between the reflection and transmission configurations), BPM-enhanced THG at 3500 nm is expected to reach 6.5×10^{-4} at 0.17 TW/cm^2, which is over one order of magnitude higher than that of other 2D materials and metasurfaces (tables S1 and S2). Compared to monolayer graphene (*12*), this structure offers advantages in terms of the higher efficiency and a broader spectral range (3000 to 5000 nm) along with higher $\chi_{\mathrm{eff}}^{(3)}$. In addition, BPM resonance can be tuned across the MIR region by designing geometric parameters, as demonstrated by BPMs with a resonance at around 3000 nm, achieving over two orders of enhancement (figs. S18 and S19).

DISCUSSION

In this work, we have investigated MIR parametric processes through the THG response in both BP and BPM structures. Our results

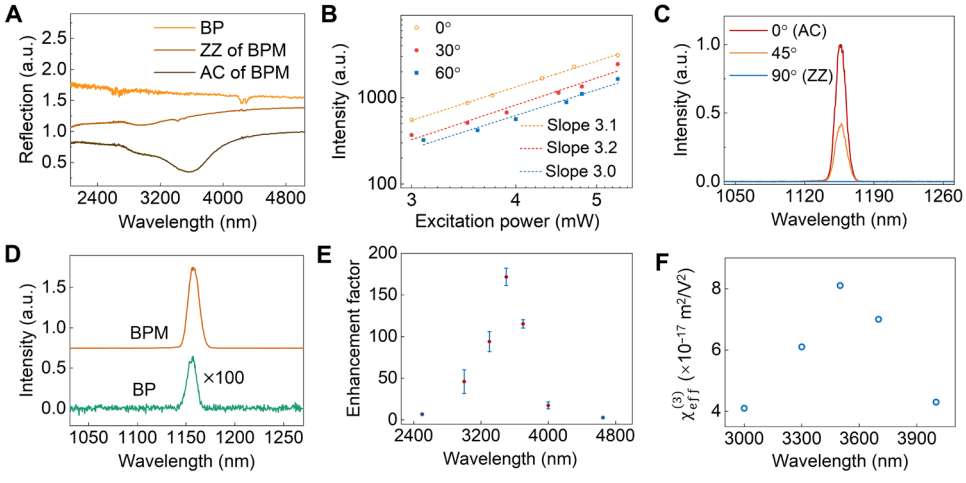

Fig. 5. THG enhancement in the BPM. (**A**) Experimental reflection spectra from the pure BP flake and the BPM. (**B**) Power-dependent THG intensity from the BPM with different polarization angles relative to the AC direction of BP. (**C**) THG intensity with different polarization angles relative to the AC direction of BP. (**D**) Measured THG spectra from the BP flake and the BPM under 3500-nm excitation. (**E**) THG enhancement as a function of the fundamental wavelength. (**F**) $\chi_{\mathrm{eff}}^{(3)}$ of BP by the plasmonic enhancement versus the fundamental wavelength.

reveal that BP exhibits exceptionally high third-order nonlinear susceptibility $(\chi^{(3)})$ values exceeding 10^{-18} m^2/V^2 in the MIR range, with a broadband spectral range from 3000 to 5000 nm. This enhancement is attributed to the combined contributions from the interband and intraband transition resonances, leading to multiphoton resonance. The magnitude of the $\chi^{(3)}$ value continues to increase as the wavelength increases, reaching a maximum of 1.55×10^{-17} m^2/V^2 at 5000 nm. The high THG conversion efficiency of BP, reaching the 10^{-5} range under 4000-nm excitation, represents the highest reported value among all 2D materials. One reason for BP's high conversion efficiency is its ability to maintain an ultrahigh nonlinear coefficient even with a large flake thickness. While other monolayer 2D materials (e.g., graphene and MoS_2) also exhibit ultrahigh nonlinear coefficients, their conversion efficiencies are not as high as that of BP. In addition, BP's strong optical anisotropy, in particular its large χ_{11} component along the AC direction, result in extreme polarization anisotropy for THG, which is comparable in magnitude to that observed in 1D carbon nanotubes (*38*). Theoretical modeling further demonstrates that χ_{22} is negligible relative to χ_{11} in the MIR region (3500 to 5000 nm). This anisotropic nonlinear response holds potential for applications in polarization-sensitive MIR upconversion detection (*44*) and nonlinear imaging with polarization functionality (*25*).

To further enhance THG performance and increase the effective nonlinear coefficient $(\chi^{(3)}_{eff})$ of BP, we design and fabricate BPMs. The BPM exhibits plasmonic electric field enhancement and an increased light-matter interaction mode volume, leading to a remarkable ~170-fold enhancement in THG at 3500 nm, compared to a BP flake. Moreover, broadband THG enhancement is demonstrated, with $\chi^{(3)}_{eff}$ exceeding 10^{-17} m^2/V^2 from 3000 to 5000 nm. The extraordinary plasmonic-induced enhancement results in a THG conversion efficiency of 6.5×10^{-4} at 3500 nm, which is over one order of magnitude higher than that achieved with other 2D materials and metasurfaces. Compared to all-dielectric nanostructures (*30*, *45*, *46*), plasmonic nanostructures offer advantageous broadband enhancement, making them highly promising for MIR nonlinear photonics. Further optimization of BPM geometrical parameters could further enhance THG performance. Given these findings, the demonstrated high-performance MIR parametric nonlinear processes in BP and the BPM paves the way for advancing MIR nanoscale nonlinear photonic devices.

MATERIALS AND METHODS

Sample preparation and device fabrication

The BP crystal was purchased from HQ Graphene and mechanically exfoliated onto polydimethylsiloxane stamps using blue Nitto tape. The exfoliated BP flakes were then transferred onto BaF_2 or Au substrates and subsequently encapsulated with a ~7-nm Al_2O_3 coating, which was grown using atomic layer deposition (ALD) at 250°C within 2 min.

The BPM was fabricated using a standard lift-off process. First, a 150-nm-thick Au reflective layer was deposited onto a Si substrate via electron-beam evaporation (AJA ebeam evaporator). After transferring the BP flake onto the Au layer, a 7-nm Al_2O_3 encapsulation was deposited to protect the BP surface. The designed metasurface pattern was then defined by using electron-beam lithography (JEOL 6300FS), followed by the deposition of a 5-nm Ti/50-nm Au layer onto the polymethyl methacrylate pattern after the developing process. The metasurface structure was fabricated via the lift-off process. The Al_2O_3 encapsulation plays a crucial role in preventing damage and corrugation of the BP surface (fig. S23).

Sample and device characterization

The thickness of the BP flake was measured using an AFM system (Park NX10). High-resolution Raman spectra were obtained using a confocal Raman microscopy system (WITec CRM200). The samples were excited with a 532-nm laser through an objective [×100, numerical aperture (NA) = 0.8], and the Raman signal was analyzed using a spectrometer integrated with a cooled charge-coupled device (CCD). The MIR absorption spectra of the BP flakes were measured by a Fourier transform infrared (FTIR) spectrometer (Bruker) equipped with a cooled mercury cadmium telluride (MCT) detector (InfraRed Associates). A broadband polarized light source, produced by filtering the emission of an 800-K blackbody (wavelength range, 0.7 to 18 μm) through a broadband polarizer, was used as an incident light for reflection and absorption measurements. The absorption spectra were obtained by comparing the transmission spectra of the BP flakes with those of the BaF_2 substrate. The polarized absorption of BP was measured by rotating the polarizer in the incident light path. The reflection spectra of the BPM were measured by the FTIR spectrometer equipped with a cooled MCT detector. The reflection spectra were calculated using the equation: $R = R_{BPM} / R_{sub}$, where R_{BPM} represents the reflection from the BPM and R_{sub} is the reflection from the Au substrate.

Numerical simulations

The numerical simulations were performed with commercial FDTD software (Lumerical FDTD Solutions). The excitation source was a normal incident plane wave along the *z* direction. To ensure accurate boundary conditions, perfectly matched layers were applied along the *z* direction, and periodic boundary conditions were introduced in the *x* (AC) and *y* (ZZ) directions. The optical constants of BP were taken from (*34*), while those of Au and Al_2O_3 were taken from the Lumerical software database.

Nonlinear optical measurement

The nonlinear optical activities were measured using a home-built optical setup in both reflection and transmission configurations (Fig. 2A). A home-built optical parametric amplifier pumped by a mode-locked femtosecond (fs) laser (Amplitude-Yuja, 1030 nm, 100 kHz, 400 fs) was used as the excitation source with a tunable wavelength range of 1350 nm to 5000 nm. For NIR excitation, an objective (×50, NA = 0.45) was used to excite the samples. The THG signals were collected by another objective (×20, NA = 0.45) and analyzed with a spectrometer (Kymera 328i Spectrograph) integrated with a cooled Si CCD. A reflective objective (LMM40X-P01) was used for MIR power-dependent, wavelength-dependent, and thickness-dependent measurements. For MIR polarization-dependent and metasurface measurements, a MIR lens (Edmund) with a focal length of ~12.7 mm was used to focus the fundamental light onto the samples. The transmitted THG signals were collected by another objective (×20, NA = 0.45), and the reflected THG signals were collected by the sample lens. The collected signals were analyzed by a spectrometer integrated with a cooled InGaAs CCD. To measure the angle-dependent THG, half-wave plates were used to control the polarization of the fundamental light.

Wavelength-dependent THG measurements require calibrating the optical setup's wavelength-dependent losses, which arise from the objective, filter, focus lens, fiber, grating, and CCD quantum efficiency. The spectral response in the THG spectral range was calibrated using a standard calibrated light source (AVALIGHT-HAL-CAL-MINI).

Estimation of third-order susceptibilities ($\chi^{(3)}$)

The third-order nonlinear susceptibility $\left(\chi^{(3)}\right)$ was estimated using the following equation for average THG power ($P_{3\omega}$) as a function of the incident average power (P_{ω}) (*21*)

$$P_{3\omega} = \frac{9\omega^2 l^2 |\chi^{(3)}|^2}{16 |\tilde{n}_{3\omega}| n_{\omega}^3 \epsilon_0^2 c^4} \frac{P_{\omega}^3}{f_{\text{rep}}^2 W^4 \tau^2 \left(\frac{\pi}{4\ln 2}\right)^3} \left[\frac{e^{-2\alpha l} - 2\cos(\Delta k l) e^{-\alpha l} + 1}{\alpha^2 l^2 + \Delta k^2 l^2}\right] e^{-2\alpha l} \quad (2)$$

where ω is the fundamental frequency, l (typically ~20 nm) is the BP thickness, which is much smaller than L_{coh} of BP, P_{ω} and $P_{3\omega}$ are the average excitation and THG powers inside the sample, respectively, $|\tilde{n}_{3\omega}|$ represents the complex RI of BP at the THG wavelength, n_{ω} is the real part of the complex RI of BP at the fundamental wavelength, $\Delta k = \frac{6\pi(n_{\omega} - n_{3\omega})}{\lambda_1}$ is the phase-mismatch between the fundamental light and the forward THG light, where λ_1 is the fundamental wavelength. Optical constants of BP are extracted from (*34*), where $\varepsilon_0 \approx 8.85 \times 10^{-12}$ F/m is the vacuum permittivity, $c = 3 \times 10^8$ m/s is the velocity of light in the vacuum, $f_{\text{rep}} = 100$ kHz is the laser repetition frequency, $\tau \approx 600$ fs is the pulse duration, $\alpha = \frac{2\pi\kappa}{\lambda_3}$ is related to the absorption coefficient of BP at the THG wavelength, where κ and λ_3 are the imaginary part of RI and the THG wavelength, respectively (*34*). The focused beam diameter W (full width at half maximum ≈ 30 μm) was estimated using the knife-edge technique (*47*) (note S11 and fig. S24). Before performing measurements, we also calibrated the response of the spectrometer using lasers working at corresponding THG wavelengths. Interface reflectivities (BP surface, surface of the BaF_2 substrate, and surface of the Al_2O_3 film) were also taken into account in the estimation (note S12 and fig. S25). The $\chi^{(3)}$ value of BP at 1550 nm was also estimated by comparing it with monolayer MoS_2, using the following expression (*22*): $\chi^{(3)}_{\text{BP}} = \frac{l_{\text{MoS}_2}}{l_{\text{BP}}} \sqrt{\frac{I_{\text{BP}}(3\omega)}{I_{\text{MoS}_2}(3\omega)}} \sqrt{\frac{I^3_{\text{MoS}_2}(\omega)}{I^3_{\text{BP}}(\omega)}} \chi^{(3)}_{\text{MoS}_2}$ ($\chi^{(3)}_{\text{MoS}_2} = 3.6 \times 10^{-19}$ m^2/V^2 in table S1 and fig. S26), where l_{MoS_2} and l_{BP} are thicknesses of monolayer MoS_2 and BP, respectively, $I_{\text{MoS}_2}(3\omega)$ and $I_{\text{BP}}(3\omega)$ are THG intensities from MoS_2 and BP, respectively, $I_{\text{MoS}_2}(\omega)$ and $I_{\text{BP}}(\omega)$ are excitation intensities in MoS_2 and BP, respectively.

Supplementary Materials

This PDF file includes:

Notes S1 to S13
Figs. S1 to S27
Tables S1 and S2
References

REFERENCES AND NOTES

1. N. L. B. Sayson, T. Bi, V. Ng, H. Pham, L. S. Trainor, H. G. L. Schwefel, S. Coen, M. Erkintalo, S. G. Murdoch, Octave-spanning tunable parametric oscillation in crystalline Kerr microresonators. *Nat. Photonics* **13**, 701–706 (2019).
2. K. Huang, J. Fang, M. Yan, E. Wu, H. Zeng, Wide-field mid-infrared single-photon upconversion imaging. *Nat. Commun.* **13**, 1077 (2022).
3. G. Ycas, F. R. Giorgetta, E. Baumann, I. Coddington, D. Herman, S. A. Diddams, N. R. Newbury, High-coherence mid-infrared dual-comb spectroscopy spanning 2.6 to 5.2 μm. *Nat. Photonics* **12**, 202–208 (2018).
4. J. F. Kinder, F. Cipura, T. Halfmann, Detection of HCl molecules by resonantly enhanced third-harmonic generation, driven by midinfrared laser pulses. *Phys. Rev. A* **103**, 052808 (2021).
5. S. Park, J. Yu, G. Boehm, M. A. Belkin, J. Lee, Electrically tunable third-harmonic generation using intersubband polaritonic metasurfaces. *Light Sci. Appl.* **13**, 169 (2024).
6. Z. Zheng, L. Xu, L. Huang, D. Smirnova, K. Z. Kamali, A. Yousefi, F. Deng, R. Camacho-Morales, C. Ying, A. E. Miroshnichenko, Third-harmonic generation and imaging with resonant Si membrane metasurface. *Opto-Electron. Adv.* **6**, 220174 (2023).
7. M. P. Fischer, A. Riede, K. Gallacher, J. Frigerio, G. Pellegrini, M. Ortolani, D. J. Paul, G. Isella, A. Leitenstorfer, P. Biagioni, D. Brida, Plasmonic mid-infrared third harmonic generation in germanium nanoantennas. *Light Sci. Appl.* **7**, 106 (2018).
8. F. Yue, R. Piccoli, M. Y. Shalaginov, T. Gu, K. A. Richardson, R. Morandotti, J. Hu, L. Razzari, Nonlinear mid-infrared metasurface based on a phase-change material. *Laser Photonics Rev.* **15**, 2000373 (2021).
9. O. Dogadov, C. Trovatello, B. Yao, G. Soavi, G. Cerullo, Parametric nonlinear optics with layered materials and related heterostructures. *Laser Photonics Rev.* **16**, 2100726 (2022).
10. Q. Guo, X.-Z. Qi, L. Zhang, M. Gao, S. Hu, W. Zhou, W. Zang, X. Zhao, J. Wang, B. Yan, M. Xu, Y.-K. Wu, G. Eda, Z. Xiao, S. A. Yang, H. Gou, Y. P. Feng, G.-C. Guo, W. Zhou, X.-F. Ren, C.-W. Qiu, S. J. Pennycook, A. T. S. Wee, Ultrathin quantum light source with van der Waals $NbOCl_2$ crystal. *Nature* **613**, 53–59 (2023).
11. H. Tang, Y. Wang, X. Ni, K. Watanabe, T. Taniguchi, P. Jarillo-Herrero, S. Fan, E. Mazur, A. Yacoby, Y. Cao, On-chip multi-degree-of-freedom control of two-dimensional materials. *Nature* **632**, 1038–1044 (2024).
12. G. Soavi, G. Wang, H. Rostami, D. G. Purdie, D. De Fazio, T. Ma, B. Luo, J. Wang, A. K. Ott, D. Yoon, S. A. Bourelle, J. E. Muench, I. Goykhman, S. Dal Conte, M. Celebrano, A. Tomadin, M. Polini, G. Cerullo, A. C. Ferrari, Broadband, electrically tunable third-harmonic generation in graphene. *Nat. Nanotechnol.* **13**, 583–588 (2018).
13. S. Zhu, R. Duan, W. Chen, F. Wang, J. Han, X. Xu, L. Wu, M. Ye, F. Sun, S. Han, X. Zhao, C. S. Tan, H. Liang, Z. Liu, Q. J. Wang, Ultrastrong optical harmonic generations in layered platinum disulfide in the mid-infrared. *ACS Nano* **17**, 2148–2158 (2023).
14. L. Yue, C. Liu, S. Han, H. Hong, Y. Wang, Q. Liu, J. Qi, Y. Li, D. Wu, K. Liu, E. Wang, T. Dong, N. Wang, Giant nonlinear optical wave mixing in a van der Waals correlated insulator. *Sci. Adv.* **10**, eadn6216 (2024).
15. A. Autere, H. Jussila, Y. Dai, Y. Wang, H. Lipsanen, Z. Sun, Nonlinear optics with 2D layered materials. *Adv. Mater.* **30**, e1705963 (2018).
16. Y. Zhang, B. Gao, D. Lepage, Y. Tong, P. Wang, W. Xia, J. Niu, Y. Feng, H. Chen, H. Qian, Large second-order susceptibility from a quantized indium tin oxide monolayer. *Nat. Nanotechnol.* **19**, 463–470 (2024).
17. Y. Zhu, Y. Wang, X. Pang, Y. Jiang, X. Liu, Q. Li, Z. Wang, C. Liu, W. Hu, P. Zhou, Non-volatile 2D MoS_2/black phosphorus heterojunction photodiodes in the near- to mid-infrared region. *Nat. Commun.* **15**, 6015 (2024).
18. R. Peng, K. Khaliji, N. Youngblood, R. Grassi, T. Low, M. Li, Midinfrared electro-optic modulation in few-layer black phosphorus. *Nano Lett.* **17**, 6315–6320 (2017).
19. H. Kim, S. Z. Uddin, D.-H. Lien, M. Yeh, N. S. Azar, S. Balendhran, T. Kim, N. Gupta, Y. Rho, C. P. Grigoropoulos, K. B. Crozier, A. Javey, Actively variable-spectrum optoelectronics with black phosphorus. *Nature* **596**, 232–237 (2021).
20. C. Chen, X. Lu, B. Deng, X. Chen, Q. Guo, C. Li, C. Ma, S. Yuan, E. Sung, K. Watanabe, T. Taniguchi, L. Yang, F. Xia, Widely tunable mid-infrared light emission in thin-film black phosphorus. *Sci. Adv.* **6**, eaay6134 (2020).
21. N. Youngblood, R. Peng, A. Nemilentsau, T. Low, M. Li, Layer-tunable third-harmonic generation in multilayer black phosphorus. *ACS Photonics* **4**, 8–14 (2017).
22. A. Autere, C. R. Ryder, A. Säynätjoki, L. Karvonen, B. Amirsolaimani, R. A. Norwood, N. Peyghambarian, K. Kieu, H. Lipsanen, M. C. Hersam, Z. Sun, Rapid and large-area characterization of exfoliated black phosphorus using third-harmonic generation microscopy. *J. Phys. Chem. Lett.* **8**, 1343–1350 (2017).
23. M. J. L. F. Rodrigues, C. J. S. de Matos, Y. W. Ho, H. Peixoto, R. E. P. de Oliveira, H.-Y. Wu, A. H. C. Neto, J. Viana-Gomes, Resonantly increased optical frequency conversion in atomically thin black phosphorus. *Adv. Mater.* **28**, 10693–10700 (2016).
24. I. Alonso Calafell, L. A. Rozema, D. Alcaraz Iranzo, A. Trenti, P. K. Jenke, J. D. Cox, A. Kumar, H. Bieliaiev, S. Nanot, C. Peng, D. K. Efetov, J.-Y. Hong, J. Kong, D. R. Englund, F. J. García de Abajo, F. H. L. Koppens, P. Walther, Giant enhancement of third-harmonic generation in graphene–metal heterostructures. *Nat. Nanotechnol.* **16**, 318–324 (2021).
25. G. Li, S. Zhang, T. Zentgraf, Nonlinear photonic metasurfaces. *Nat. Rev. Mater.* **2**, 17010 (2017).
26. G. Q. Ngo, E. Najafidehaghani, Z. Gan, S. Khazaee, M. P. Siems, A. George, E. P. Schartner, S. Nolte, H. Ebendorff-Heidepriem, T. Pertsch, A. Tuniz, M. A. Schmidt, U. Peschel, A. Turchanin, F. Eilenberger, In-fibre second-harmonic generation with embedded two-dimensional materials. *Nat. Photonics* **16**, 769–776 (2022).
27. Y. Zuo, W. Yu, C. Liu, X. Cheng, R. Qiao, J. Liang, X. Zhou, J. Wang, M. Wu, Y. Zhao, P. Gao, S. Wu, Z. Sun, K. Liu, X. Bai, Z. Liu, Optical fibres with embedded two-dimensional materials for ultrahigh nonlinearity. *Nat. Nanotechnol.* **15**, 987–991 (2020).
28. C.-Y. Zhu, Z. Zhang, J.-K. Qin, Z. Wang, C. Wang, P. Miao, Y. Liu, P.-Y. Huang, Y. Zhang, K. Xu, L. Zhen, Y. Chai, C.-Y. Xu, Two-dimensional semiconducting SnP_2Se_6 with giant

second-harmonic-generation for monolithic on-chip electronic-photonic integration. *Nat. Commun.* **14**, 2521 (2023).
29. J. Zhao, A. Fieramosca, R. Bao, W. Du, K. Dini, R. Su, J. Feng, Y. Luo, D. Sanvitto, T. C. H. Liew, Q. Xiong, Nonlinear polariton parametric emission in an atomically thin semiconductor based microcavity. *Nat. Nanotechnol.* **17**, 396–402 (2022).
30. G. Zograf, A. Y. Polyakov, M. Bancerek, T. J. Antosiewicz, B. Küçüköz, T. O. Shegai, Combining ultrahigh index with exceptional nonlinearity in resonant transition metal dichalcogenide nanodisks. *Nat. Photonics* **18**, 751–757 (2024).
31. J. Lee, M. Tymchenko, C. Argyropoulos, P.-Y. Chen, F. Lu, F. Demmerle, G. Boehm, M.-C. Amann, A. Alù, M. A. Belkin, Giant nonlinear response from plasmonic metasurfaces coupled to intersubband transitions. *Nature* **511**, 65–69 (2014).
32. J. Yu, S. Park, I. Hwang, D. Kim, F. Demmerle, G. Boehm, M.-C. Amann, M. A. Belkin, J. Lee, Electrically tunable nonlinear polaritonic metasurface. *Nat. Photonics* **16**, 72–78 (2022).
33. J. Yu, S. Park, I. Hwang, D. Kim, J.-Y. Jung, J. Lee, Third-harmonic generation from plasmonic metasurfaces coupled to intersubband transitions. *Adv. Opt. Mater.* **7**, 1801510 (2019).
34. J. Bullock, M. Amani, J. Cho, Y.-Z. Chen, G. H. Ahn, V. Adinolfi, V. R. Shrestha, Y. Gao, K. B. Crozier, Y.-L. Chueh, A. Javey, Polarization-resolved black phosphorus/molybdenum disulfide mid-wave infrared photodiodes with high detectivity at room temperature. *Nat. Photonics* **12**, 601–607 (2018).
35. D. Hähnel, C. Golla, M. Albert, T. Zentgraf, V. Myroshnychenko, J. Förstner, C. Meier, A multi-mode super-fano mechanism for enhanced third harmonic generation in silicon metasurfaces. *Light Sci. Appl.* **12**, 97 (2023).
36. F. Bijloo, K. Murzyn, F. van Emmerik, A. J. den Boef, P. M. Kraus, A. F. Koenderink, Near-unity all-optical modulation of third-harmonic generation with a Fano-resonant dielectric metasurface. *Nano Lett.* **24**, 12942–12947 (2024).
37. S. Biswas, M. Y. Grajower, K. Watanabe, T. Taniguchi, H. A. Atwater, Broadband electro-optic polarization conversion with atomically thin black phosphorus. *Science* **374**, 448–453 (2021).
38. S. Zhu, W. Li, S. Yu, N. Komatsu, A. Baydin, F. Wang, F. Sun, C. Wang, W. Chen, C. S. Tan, H. Liang, Y. Yomogida, K. Yanagi, J. Kono, Q. J. Wang, Extreme polarization anisotropy in resonant third-harmonic generation from aligned carbon nanotube films. *Adv. Mater.* **35**, e2304082 (2023).
39. L. Li, J. Kim, C. Jin, G. J. Ye, D. Y. Qiu, F. H. da Jornada, Z. Shi, L. Chen, Z. Zhang, F. Yang, K. Watanabe, T. Taniguchi, W. Ren, S. G. Louie, X. H. Chen, Y. Zhang, F. Wang, Direct observation of the layer-dependent electronic structure in phosphorene. *Nat. Nanotechnol.* **12**, 21–25 (2017).
40. A. Saynatjoki, L. Karvonen, H. Rostami, A. Autere, S. Mehravar, A. Lombardo, R. A. Norwood, T. Hasan, N. Peyghambarian, H. Lipsanen, K. Kieu, A. C. Ferrari, M. Polini, Z. Sun, Ultra-strong nonlinear optical processes and trigonal warping in MoS_2 layers. *Nat. Commun.* **8**, 893 (2017).
41. S. Zhu, R. Duan, X. Xu, F. Sun, W. Chen, F. Wang, S. Li, M. Ye, X. Zhou, J. Cheng, Y. Wu, H. Liang, J. Kono, X. Li, Z. Liu, Q. J. Wang, Strong nonlinear optical processes with extraordinary polarization anisotropy in inversion-symmetry broken two-dimensional PdPSe. *Light Sci. Appl.* **13**, 119 (2024).
42. D. P. Fromm, A. Sundaramurthy, P. J. Schuck, G. Kino, W. Moerner, Gap-dependent optical coupling of single "bowtie" nanoantennas resonant in the visible. *Nano Lett.* **4**, 957–961 (2004).
43. Y. Dai, Y. Wang, S. Das, S. Li, H. Xue, A. Mohsen, Z. Sun, Broadband plasmon-enhanced four-wave mixing in monolayer MoS_2. *Nano Lett.* **21**, 6321–6327 (2021).
44. P. Liu, L. Guo, F. Qi, W. Li, W. Li, Q. Fu, J. Yao, M. Xia, Z. Liu, Y. Wang, Large dynamic range and wideband mid-infrared upconversion detection with $BaGa_4Se_7$ crystal. *Optica* **9**, 50–55 (2022).
45. A. Di Francescantonio, A. Zilli, D. Rocco, V. Vinel, L. Coudrat, F. Conti, P. Biagioni, L. Duò, A. Lemaître, C. De Angelis, G. Leo, M. Finazzi, M. Celebrano, All-optical free-space routing of upconverted light by metasurfaces via nonlinear interferometry. *Nat. Nanotechnol.* **19**, 298–305 (2024).
46. K. Koshelev, S. Kruk, E. Melik-Gaykazyan, J.-H. Choi, A. Bogdanov, H.-G. Park, Y. Kivshar, Subwavelength dielectric resonators for nonlinear nanophotonics. *Science* **367**, 288–292 (2020).
47. M. A. De Araújo, R. Silva, E. De Lima, D. P. Pereira, P. C. De Oliveira, Measurement of Gaussian laser beam radius using the knife-edge technique: Improvement on data analysis. *Appl. Optics* **48**, 393–396 (2009).
48. J. Heyd, G. E. Scuseria, M. Ernzerhof, Hybrid functionals based on a screened Coulomb potential. *J. Chem. Phys.* **118**, 8207–8215 (2003).
49. G. Kresse, J. Furthmüller, Efficient iterative schemes for ab initio total-energy calculations using a plane-wave basis set. *Phys. Rev. B Condens. Matter.* **54**, 11169–11186 (1996).
50. P. E. Blöchl, Projector augmented-wave method. *Phys. Rev. B* **50**, 17953–17979 (1994).
51. J. Klimeš, D. R. Bowler, A. Michaelides, Van der Waals density functionals applied to solids. *Phys. Rev. B* **83**, 195131 (2011).
52. A. Brown, S. Rundqvist, Refinement of the crystal structure of black phosphorus. *Acta Crystallogr.* **19**, 684–685 (1965).
53. A. A. Mostofi, J. R. Yates, Y.-S. Lee, I. Souza, D. Vanderbilt, N. Marzari, wannier90: A tool for obtaining maximally-localised Wannier functions. *Comput. Phys. Commun.* **178**, 685–699 (2008).
54. C. Aversa, J. E. Sipe, Nonlinear optical susceptibilities of semiconductors: Results with a length-gauge analysis. *Phys. Rev. B* **52**, 14636–14645 (1995).
55. R. W. Boyd, *Nonlinear Optics* (Academic Press, 2008).
56. V. A. Margulis, T. Sizikova, Theoretical study of third-order nonlinear optical response of semiconductor carbon nanotubes. *Phys. B Condens. Matter* **245**, 173–189 (1998).
57. Y. Yang, W. Wang, A. Boulesbaa, I. I. Kravchenko, D. P. Briggs, A. Puretzky, D. Geohegan, J. Valentine, Nonlinear Fano-resonant dielectric metasurfaces. *Nano Lett.* **15**, 7388–7393 (2015).
58. H. Choo, M.-K. Kim, M. Staffaroni, T. J. Seok, J. Bokor, S. Cabrini, P. J. Schuck, M. C. Wu, E. Yablonovitch, Nanofocusing in a metal-insulator-metal gap plasmon waveguide with a three-dimensional linear taper. *Nat. Photonics* **6**, 838–844 (2012).
59. X. Ling, H. Wang, S. Huang, F. Xia, M. S. Dresselhaus, The renaissance of black phosphorus. *Proc. Natl. Acad. Sci. U.S.A.* **112**, 4523–4530 (2015).
60. Q. Cui, R. A. Muniz, J. Sipe, H. Zhao, Strong and anisotropic third-harmonic generation in monolayer and multilayer ReS_2. *Phys. Rev. B* **95**, 165406 (2017).
61. A. Dasgupta, J. Gao, X. Yang, Anisotropic third-harmonic generation in layered germanium selenide. *Laser Photonics Rev.* **14**, 1900416 (2020).
62. A. Autere, H. Jussila, A. Marini, J. Saavedra, Y. Dai, A. Säynätjoki, L. Karvonen, H. Yang, B. Amirsolaimani, R. A. Norwood, N. Peyghambarian, H. Lipsanen, K. Kieu, F. J. G. de Abajo, Z. Sun, Optical harmonic generation in monolayer group-VI transition metal dichalcogenides. *Phys. Rev. B* **98**, 115426 (2018).
63. R. I. Woodward, R. T. Murray, C. F. Phelan, R. E. P. de Oliveira, T. H. Runcorn, E. J. R. Kelleher, S. Li, E. C. de Oliveira, G. J. M. Fechine, G. Eda, C. J. S. de Matos, Characterization of the second- and third-order nonlinear optical susceptibilities of monolayer MoS_2 using multiphoton microscopy. *2D Mater.* **4**, 011006 (2017).
64. A. A. Popkova, I. M. Antropov, J. E. Fröch, S. Kim, I. Aharonovich, V. O. Bessonov, A. S. Solntsev, A. A. Fedyanin, Optical third-harmonic generation in hexagonal boron nitride thin films. *ACS Photonics* **8**, 824–831 (2021).
65. Y. Xiang, C. Yan, T. D. Stanescu, Y. Ma, R. Sooriyagoda, F. Shi, A. D. Bristow, L. Li, C. Cen, Giant third-harmonic optical generation from topological insulator heterostructures. *Nano Lett.* **21**, 8872–8879 (2021).
66. L. Du, Y. Zhao, L. Wu, X. Hu, L. Yao, Y. Wang, X. Bai, Y. Dai, J. Qiao, M. G. Uddin, X. Li, J. Lahtinen, X. Bai, G. Zhang, W. Ji, Z. Sun, Giant anisotropic photonics in the 1D van der Waals semiconductor fibrous red phosphorus. *Nat. Commun.* **12**, 4822 (2021).
67. T. Ning, O. Hyvärinen, H. Pietarinen, T. Kaplas, M. Kauranen, G. Genty, Third-harmonic UV generation in silicon nitride nanostructures. *Opt. Express* **21**, 2012–2017 (2013).
68. U. Gubler, C. Bosshard, Optical third-harmonic generation of fused silica in gas atmosphere: Absolute value of the third-order nonlinear optical susceptibility $\chi^{(3)}$. *Phys. Rev. B* **61**, 10702–10710 (2000).
69. N. K. Hon, R. Soref, B. Jalali, The third-order nonlinear optical coefficients of Si, Ge, and $Si_{1-x}Ge_x$ in the midwave and longwave infrared. *J. Appl. Phys.* **110**, 011301 (2011).
70. H. Kobayashi, H. Kanbara, M. Koga, K. Kubodera, Third-order nonlinear optical properties of As_2S_3 chalcogenide glass. *J. Appl. Phys.* **74**, 3683–3687 (1993).
71. S. Lauria, M. F. Saleh, Mixing second- and third-order nonlinear interactions in nanophotonic lithium-niobate waveguides. *Phys. Rev. A* **105**, 043511 (2022).
72. S. Chen, M. Rahmani, K. F. Li, A. Miroshnichenko, T. Zentgraf, G. Li, D. Neshev, S. Zhang, Third harmonic generation enhanced by multipolar interference in complementary silicon metasurfaces. *ACS Photonics* **5**, 1671–1675 (2018).
73. Z. Liu, Y. Xu, Y. Lin, J. Xiang, T. Feng, Q. Cao, J. Li, S. Lan, J. Liu, High-*Q* quasibound states in the continuum for nonlinear metasurfaces. *Phys. Rev. Lett.* **123**, 253901 (2019).
74. G. Yang, S. U. Dev, M. S. Allen, J. W. Allen, H. Harutyunyan, Optical bound states in the continuum enabled by magnetic resonances coupled to a mirror. *Nano Lett.* **22**, 2001–2008 (2022).
75. Y. Gao, Y. Fan, Y. Wang, W. Yang, Q. Song, S. Xiao, Nonlinear holographic all-dielectric metasurfaces. *Nano Lett.* **18**, 8054–8061 (2018).
76. X. Wang, Z. Liu, B. Chen, G. Qiu, D. Wei, J. Liu, Experimental demonstration of high-efficiency harmonic generation in photonic Moiré superlattice microcavities. *Nano Lett.* **24**, 11327–11333 (2024).
77. O. A. M. Abdelraouf, A. P. Anthur, X. R. Wang, Q. J. Wang, H. Liu, Modal phase-matched bound states in the continuum for enhancing third harmonic generation of deep ultraviolet emission. *ACS Nano* **18**, 4388–4397 (2024).
78. H.-H. Hsiao, J.-C. Hsieh, A.-Y. Liu, K.-I. Lin, Y.-C. Hsu, Enhancement of third-harmonic generation in all-dielectric kite-shaped metasurfaces driven by quasi-bound states in the continuum. *Nanophotonics* **13**, 3155–3164 (2024).
79. O. A. M. Abdelraouf, A. P. Anthur, Z. Dong, H. Liu, Q. Wang, L. Krivitsky, X. Renshaw Wang, Q. J. Wang, H. Liu, Multistate tuning of third harmonic generation in Fano-resonant hybrid dielectric metasurfaces. *Adv. Funct. Mater.* **31**, 2104627 (2021).

80. M. Nauman, J. Yan, D. de Ceglia, M. Rahmani, K. Zangeneh Kamali, C. De Angelis, A. E. Miroshnichenko, Y. Lu, D. N. Neshev, Tunable unidirectional nonlinear emission from transition-metal-dichalcogenide metasurfaces. *Nat. Commun.* **12**, 5597 (2021).

Acknowledgments

Funding: Q.J.W. acknowledges the National Research Foundation Singapore program (grant nos. NRF-CRP23-2019-0007 and NRF-CRP29-2022-0003) and the A*STAR grant (grant nos. M22K2c0080, R23I0IR041, and M23M2b0056). T.T. acknowledges the Turing Scheme 2023-24, Imperial College London. **Author contributions:** Conceptualization: S.Z., W.C., T.T., C.Y., R.T.M., R.D., Y.L., and Q.J.W. Methodology: S.Z., W.C., T.T., X.X., R.D., C.Y., Z.L., R.T.M., and Y.L. Software: S.Z., X.X., T.W., X.M., J.Y., and J.C. Validation: S.Z., W.C., T.T., R.D., X.M., C.Y., J.C., J.L., Z.L., and Y.L. Formal analysis: S.Z., W.C., T.T., X.X., R.D., X.M., C.Y., J.C., J.Y., J.L., Y.L., and Q.J.W. Investigation: S.Z., W.C., T.T., R.D., C.Y. X.M., and C.W. Resources: S.Z., T.T., F.W., R.D., T.W., C.Y., C.W., J.C., Z.L., R.T.M., and Q.J.W. Data curation: S.Z., W.C., T.T., X.X., R.D., Y.L., and Q.J.W. Writing–original draft: S.Z. and R.D. Writing–review and editing: S.Z.,W.C., T.T., F.W., X.X., R.D., T.W., X.M., C.Y., Y.J., D.J.J., Z.L., R.T.M., and Y.L. Visualization: S.Z., W.C., R.D., T.W., X.M., C.Y., C.W., and Y.L. Supervision: R.T.M., Y.L., and Q.J.W. Project administration: R.T.M., Y.L., and Q.J.W. Funding acquisition: R.T.M., Y.L., and Q.J.W. **Competing interests:** The authors declare that they have no competing interests. **Data and materials availability:** All data needed to evaluate the conclusions in the paper are present in the paper and/or the Supplementary Materials.

Submitted 25 September 2024
Accepted 9 April 2025
Published 14 May 2025
10.1126/sciadv.adt3772